

See discussions, stats, and author profiles for this publication at: <https://www.researchgate.net/publication/255950868>

Direct Imaging of Atomic Scale Structure and Electronic Properties of GaAs Wurtzite and Zinc Blende Nanowire Surfaces

ARTICLE in NANO LETTERS · AUGUST 2013

Impact Factor: 13.59 · DOI: 10.1021/nl402424x · Source: PubMed

CITATIONS

24

READS

55

8 AUTHORS, INCLUDING:



[Sebastian Lehmann](#)

Lund University

69 PUBLICATIONS 391 CITATIONS

[SEE PROFILE](#)



[Rainer Timm](#)

Lund University

55 PUBLICATIONS 610 CITATIONS

[SEE PROFILE](#)



[Edvin Lundgren](#)

Lund University

231 PUBLICATIONS 5,800 CITATIONS

[SEE PROFILE](#)



[Anders Mikkelsen](#)

Lund University

156 PUBLICATIONS 2,795 CITATIONS

[SEE PROFILE](#)

Direct Imaging of Atomic Scale Structure and Electronic Properties of GaAs Wurtzite and Zinc Blende Nanowire Surfaces

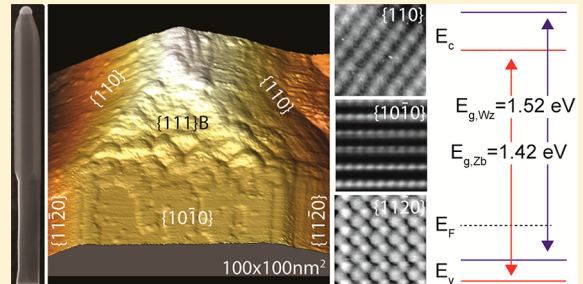
M. Hjort,[†] S. Lehmann,[†] J. Knutsson,[†] R. Timm,[†] D. Jacobsson,[†] E. Lundgren,[†] K.A. Dick,^{†,‡} and A. Mikkelsen^{*,†}

[†]Department of Physics, Lund University, P.O. Box 118, 22 100 Lund, Sweden

[‡]Department of Chemistry, Lund University, P.O. Box 124, 221 00 Lund, Sweden

Supporting Information

ABSTRACT: Using scanning tunneling microscopy and spectroscopy we study the atomic scale geometry and electronic structure of GaAs nanowires exhibiting controlled axial stacking of wurtzite (Wz) and zinc blende (Zb) crystal segments. We find that the nonpolar low-index surfaces {110}, {10̄10}, and {11̄20} are unreconstructed, unpinned, and without states in the band gap region. Direct comparison between Wz and Zb GaAs reveal a type-II band alignment and a Wz GaAs band gap of 1.52 eV



KEYWORDS: STM, nanowire, surface, III–V, GaAs, STS

GaAs is easily the most commonly used materials system for III–V based electronics. Recently an upsurge of new and interesting nanowire (NW) structures has also been realized based on GaAs.^{1–3} A prerequisite for the use of GaAs NWs in device structures is to have materials of very high crystal quality. Because of recent advances, it has become possible to grow pure zinc blende (Zb) and pure wurtzite (Wz) NWs⁴ as well as heterostructures with axial switching between Zb and Wz segments.^{5–7} Beyond achieving crucial crystal perfection, such nanostructures can also be used for fundamental studies of the isolated influence of crystal structure on physical and chemical properties and may allow for engineered applications such as crystal phase quantum dots.^{8–11} Despite considerable efforts, there is still a controversy over band gap energy and band ordering in the GaAs nanowire system. Band gap energy in bulk Zb GaAs is well-known, but the Wz band structure and the Wz-Zb band offset are under debate. Experimental determination of the GaAs Wz band gap ranges from 1.44 to 1.54 eV^{12–16} whereas ab initio calculations result in band gaps between 1.38 and 1.81 eV.^{17–19} For the Wz-Zb band ordering, calculations propose a type II-staggered band alignment with varying conduction band offsets of 63,²⁰ 101,¹³ 117,¹⁸ and 149 meV.²¹

Scanning tunneling microscopy and spectroscopy (STM/S) have in recent years become applicable to III–V NW studies giving access to new important information.^{22–24} STM allows direct studies of the NW surfaces, which inherently (due to the large surface-to-volume ratio) are a necessity to control and tune to predict electronic and optical properties and even predict the growth of entire NWs.²⁴ Importantly, STM/S has previously delivered central contributions to understanding electronic properties of III–V Zb semiconductors beyond the

surface region using clean and low defect density {110}-type facets, which can be obtained in vacuum by cleaving (001) oriented wafers.²⁵ The unreconstructed and unpinned nature of these facets has made it possible to study bulk properties. STM/S with its possibilities for dopant profiling and studies of buried structures has greatly contributed to the development of III–V nanostructures.^{26–28} Until now, only a handful of studies have been presented dealing with the atomically resolved surface structure of III–V NWs^{22–24} and both electronic and structural information have been obtained, albeit not from the GaAs material system.

In the Wz phase the {10̄10}- and the {11̄20}-type facets exist, corresponding to the Zb {112}- and {110}-type equivalent surfaces. The possibilities to utilize these facets for STM studies of bulk features such as Fermi level positions and band alignments require intrinsically unreconstructed surfaces without states in the band gap as well as large and defect free terraces on the NWs. The Wz facets are also important for growth and novel devices since they adopt lower surface energies than the corresponding Zb counterparts²⁹ thus changing the growth behavior of, for example, shell materials, drastically leading to different shell properties.³⁰ The existence of such clean and unreconstructed surfaces is not a trivial matter as studies of InAs and InP NWs have shown.^{23,24}

In this Letter, we describe the first STM/S analysis of single heterostructured GaAs NWs with a well-defined axial stacking of Wz and Zb segments. The crystal structure was tuned by

Received: July 2, 2013

Revised: August 8, 2013

Published: August 13, 2013



changing the [As]/[Ga] precursor flow ratio.^{5,31} Imaging along the full length of the NWs using STM, we achieve atomic resolution on all major facets ($\{110\}$ -, $\{11\bar{2}0\}$ -, and $\{10\bar{1}0\}$ -type) as well as mapping of electronic properties using STS. We find that all the nonpolar facets are flat and unreconstructed. We obtained direct comparisons between Wz and Zb electronic structure using the same STM tip and include simulations of the tip-induced band bending (TIBB) using parameters derived from the well-known $\{110\}$ surfaces. Because of the unpinned nature of the surfaces the STS results have relevance both for the surface and bulk regions.

Single heterostructured GaAs NWs with a Wz bottom and a Zb top segment were prepared by metal–organic vapor phase epitaxy (MOVPE) following the particle-assisted growth mode and the use of Au particles. The latter were deposited onto GaAs(111) substrates by aerosol technique³² with an areal density of $1.0 \mu\text{m}^{-2}$ and 70 nm diameter. The NWs were grown at a temperature of 550 °C with trimethylgallium (TMGa) and arsine (AsH_3) as precursor materials at total reactor flows of 13 slm, and a total reactor pressure of 100 mbar. The molar fractions were set to $\chi_{\text{TMGa}} = 4.3 \times 10^{-5}$ and $\chi_{\text{AsH}_3} = 7.7 \times 10^{-5}$ and 3.9×10^{-3} for Wz and Zb conditions, respectively.^{5,31} In order to remove surface oxides and allow proper substrate preconditioning, a 10 min annealing step was carried out prior to growth at 630 °C in AsH_3/H_2 atmosphere. After that step the temperature was reduced to growth temperature, and after thermal stabilization the precursors were introduced to initiate growth. The Wz bottom segment was terminated by $\{10\bar{1}0\}$ -type facets unless overgrown at the Wz-Zb interface where $\{11\bar{2}0\}$ -type facets were formed.⁵ Mainly $\{110\}$ -type facets terminated the Zb top part except at the Wz-Zb interface where additional $\{\overline{1}\overline{1}\overline{1}\}$ -type facets were observed.^{5,31} For detailed information about the growth of sharp crystal structure interfaces in III–V NW systems, see ref 31 and references therein.

Scanning electron microscopy (SEM) characterization was carried out in a ZEISS Leo Gemini 1560 setup. For structural characterization, the nanowires were placed on copper grids covered with a lacey carbon layer and investigated in a JEOL-3000F transmission electron microscope (TEM).

The NWs were transferred to an epi-ready GaAs(111) substrate by mechanical break off and loaded into UHV for imaging and spectroscopy. After transport in air the NWs were covered in native oxide that was removed using a beam of atomic hydrogen at 550 °C for 35 min. The temperature used in the present case is slightly higher than what has previously been seen to be a suitable for atomic hydrogen cleaning of In based III–V NWs,^{23,24} due to the higher decomposition temperatures of gallium oxides. For a complete description of the sample cleaning procedure, see the Supporting Information.

The cleaned NWs were analyzed in a variable temperature Omicron XA STM, operated in ultrahigh vacuum (UHV, $P < 10^{-10}$ mbar) at room temperature. Electrochemically etched tungsten tips that had been cleaned and sharpened in vacuum by Ar-ion sputtering were used. For STS point spectra, the tip was placed at an area of interest and $I-V$ and $(dI/dV)-V$ spectra were recorded simultaneously. For the $(dI/dV)-V$ measurements, showing the differential conductivity, a lock-in technique was used with a modulation amplitude of $V_{\text{mod}} = 80$ mV and a modulation frequency of $f_{\text{mod}} = 1.1$ kHz. To increase the dynamic range of the STS measurements at the band edges, the tip–sample separation was decreased with decreasing absolute value of the bias voltage by $\sim 2 \text{ \AA/V}$, according to the

variable gap mode.^{33,34} The obtained $(dI/dV)-V$ curves were normalized to the total conductance (I/V) broadened by an exponential function, as presented in ref 33 using a broadening width of 1.0–1.5 V. The final curve showing $(dI/dV/I/V)-V$ depicts a quantity that is proportional to the local density of states (LDOS).^{35,36}

The NWs designed for the STM measurements are shown in an SEM image in Figure 1a indicating the overall morphology

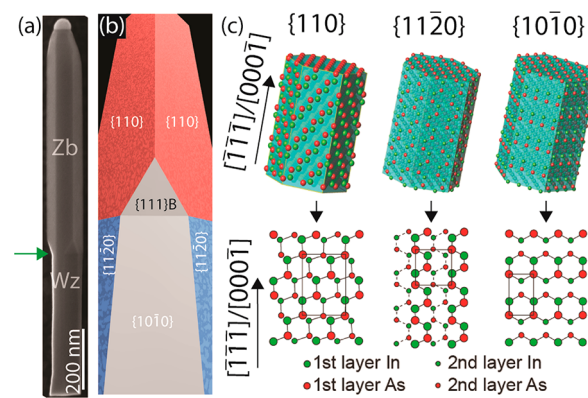


Figure 1. (a) The 30°-tilted view SEM image of a broken off, single heterostructured GaAs NW. Zinc blende (Zb) and wurtzite (Wz) parts are marked in the figure. Green arrow marks the epitaxial junction. (b) A model of the Wz-Zb interface with the facet types marked. (c) Models depicting the positions of the topmost In and As atoms in corresponding unreconstructed surfaces.

and the well-defined facets of the NW. In Figure 1b, we show a model of a NW indicating the various facets based on ref 5, and in Figure 1c we show the surface atomic scale structure of the unreconstructed surface facets.

The overall morphology of the NWs and their different facets is shown in Figure 2. Large terraces with a relatively low density of surface defects (e.g., vacancies and interstitials) could be observed; except for the small and polar interfacial $\{\overline{1}\overline{1}\overline{1}\}$ -type facet which appeared rough on the 1–2 monolayer scale. The rough $\{\overline{1}\overline{1}\overline{1}\}$ facet is due to formation of small triangular terraces in combination with a complex reconstruction pattern.³⁷ Even for perfectly smooth $\{\overline{1}\overline{1}\overline{1}\}$ -surfaces, which can be obtained by growth parameter tuning,³⁸ we would expect surface states to pin the Fermi level due to the polar nature of the surface; thereby not revealing bulk information. Different to this, the nonpolar facets have been predicted to be unreconstructed,³⁹ and presumably unpinned, allowing for general probing of the GaAs electronic structure. For the $\{110\}$ -type facets, the number of surface defects (mainly As vacancies) increased with prolonged annealing times. The low density of defects and steps is crucial in order to obtain reliable STS-data as charged defects can affect STS measurements several nanometers away.⁴⁰ Interestingly, after scanning on more than 40 NWs we have not observed any steps higher than two atomic layers and we can therefore conclude that the nonpolar NW facets are very flat and step-formation is energetically unfavorable. This is especially interesting since it indicates that the formation of the native oxide has not roughened the surface. The interfaces in between neighboring facets of the Wz and Zb parts along the axial direction were found to be atomically sharp, such as the interface between the $\{110\}$ - and the $\{11\bar{2}0\}$ -type facet in Figure 2a, which will be discussed in a later part of the paper. This allows for direct

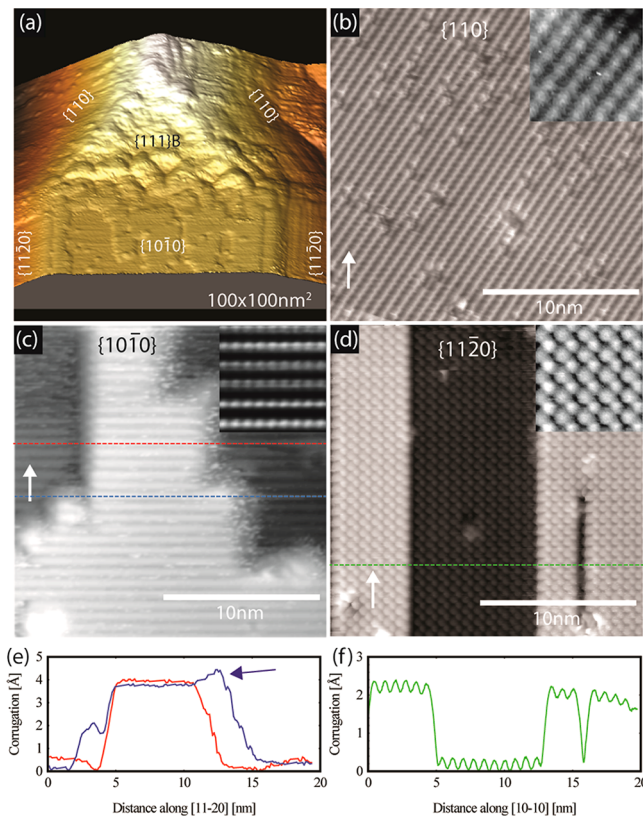


Figure 2. STM results from a single heterostructured GaAs NW. (a) The interface between the Wz (bottom) and Zb (top) part with the facet types indexed. $V_t = -2.6$ V, $I_t = 100$ pA. (b–d) Morphology of the different facets as seen in STM. $V_{t,b} = -2.5$ V, $I_{t,b} = 150$ pA, $V_{t,c} = -2.7$ V, $I_{t,c} = 110$ pA, $V_{t,d} = -3.0$ V, $I_{t,d} = 150$ pA. Insets depict atomic scale images of the corresponding facets. $V_{t,b}$ inset = -2.5 V, $I_{t,b}$ inset = 100 pA, $V_{t,c}$ inset = -3.0 V, $I_{t,c}$ inset = 110 pA, $V_{t,d}$ inset = -1.9 V, $I_{t,d}$ inset = 100 pA. White arrows mark the NW growth direction ([111] or [0001]). Sizes of insets are 3.8×3.8 nm 2 . Linescans along the dotted lines in (c,d) are shown in (e,f), respectively. Blue arrow in (e) marks the signature of bound charges.

comparison in spectroscopy between the two facets. Interestingly, we could measure the profile around the circumference of the NW and found the edge between neighboring $\{11\bar{2}0\}$ and $\{10\bar{1}0\}$ -facets to consist of a small 1 nm wide microfacet in a 10° angle with the $\{10\bar{1}0\}$ surface, indicating a small $\{1\bar{1}23\}$ type facet.

Because steps on semiconductor surfaces play a major role in both surface chemical reactions and epitaxial growth, it is most desirable to study their electronic properties. Measuring height profiles over steps allows us to deduce whether or not they are charged.⁴¹ We found that the most common steps on $\{110\}$ facets (steps with a normal vector [001]) were charged, as has been observed before.⁴² Different to this, we found that two of the most common steps on the Wz facets ($\{11\bar{2}0\}$ normal vector for $\{10\bar{1}0\}$, and $\{10\bar{1}0\}$ normal vector for $\{1120\}$) were uncharged, as is evidenced by the noncurved corrugation close to the steps in Figure 2e,f. On the other hand, kink sites on the $\{1010\}$ facet were found to be charged as can be seen in the blue line profile in Figure 2e. It is interesting to note that the same kind of step charging has been observed for some II–VI Wz surfaces such as CdSe($11\bar{2}0$) and ($10\bar{1}0$),⁴³ indicating that this might be a general feature of these Wz steps.

Utilizing the high-resolution capabilities of the STM, we proceed to image down to the individual atom level on each facet combined with surface spectroscopy. When imaging the $\{110\}$ -type facets (see inset of Figure 2b), we found rows of atoms extending at 35° angle to the [111] direction. The STM images showed similar appearance to those acquired from cleaved samples that are well-known to be unreconstructed.^{44,45} We therefore believe that possible surface deterioration introduced by the deoxidation step is of minor importance. In addition, we have performed spectroscopy on the $\{110\}$ type facet and found that the spectroscopy data matched previous spectroscopy measurements from the GaAs(110) surface.³³ We return to this facet when comparing it to the Wz facets.

Turning our attention to the $\{10\bar{1}0\}$ -type facet we found that under negative sample bias images as the one in Figure 3g was obtained with circular protrusions along well-defined rows. We interpret the atomic rows extending along $[11\bar{2}0]$ as an unreconstructed surface in agreement with recent ab initio-

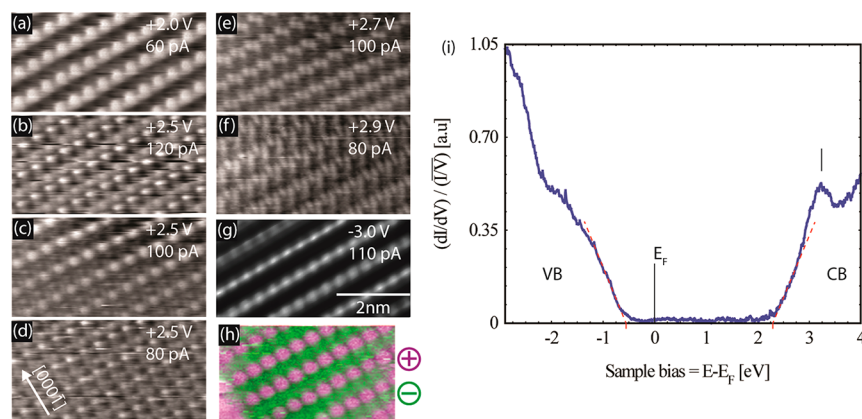


Figure 3. STM images from a $\{10\bar{1}0\}$ -type facet. (a–g) Images obtained from a $\{10\bar{1}0\}$ facet using a variety of tunneling voltage and current settings. At low positive bias, bright spots are seen with distances matching the topmost Ga-atoms. At higher bias, we detect a more elaborate pattern where the spots do not directly correspond to the top Ga or As atoms. At negative bias (g), we observe a pattern matching atomic distances of the topmost As-atoms. (h) Image obtained in dual mode where a positive and a negative bias image is obtained at the same time and then overlaid; purple is positive bias ($+2.7$ V), green is negative bias (-2.9 V). (i) STS spectrum from the $\{10\bar{1}0\}$ -type facet. The linear onsets marked by the dotted red lines show the valence and conduction band edges. States associated with tunneling out of filled valence band states, VB, and tunneling into empty conduction band states, CB, are marked as well as the Fermi level, E_F . The black line marks a surface state related feature.

calculations predicting (1×1) surfaces to be the most stable.^{29,39} Interestingly, the images obtained under negative bias only had a slight dependence on bias settings, just like at the $\{110\}$ -facet.⁴⁴ With low charge carrier concentration, it is often found that the tip-induced band bending (TIBB) in the semiconductor is too large and no carrier inversion takes place, making it impossible to tunnel into empty states.⁴⁶ However, with a sufficiently sharp tip, that is, less TIBB, we managed to obtain atomically resolved images with positive bias as is depicted in Figure 3a. At these settings ($V_t = +2.0$ V and $I_t = 60$ pA), the appearance was similar to what was seen using negative bias (filled states) with rows of well-defined spots oriented along $[11\bar{2}0]$.

At higher positive bias, Figure 3b–d, we noticed the appearance of features in between the well-defined rows. At even higher positive bias we first noticed a splitting of the spots, Figure 3e, and then moving over to a more Y-like shape, Figure 3f. The opposite behavior has been seen for GaAs(110) with additional features at low positive bias/high currents/small tip–sample separation.^{47,48} Also at fixed bias, Figure 3b–d, we note that the tunneling current had a major effect on the images. Previous studies on the GaAs(110) have shown that surface resonances play a large role in imaging using positive bias and can greatly change features in the acquired images.⁴⁴ This would be indicative of a somewhat different distribution of surface resonances for the Wz surfaces compared to the Zb.

We also imaged in so-called dual-mode where the polarity is switched sequentially when the tip is moved back and forth, thereby forming two images simultaneously with both polarities. In Figure 3h, we show such an image where we have overlaid the images colored green for negative bias (filled states) and purple for positive bias (empty states). From the image, we clearly see that the filled states and the empty states were located at different spatial positions. This is similar to the GaAs(110) surface where the empty states are mainly centered above the Ga-atoms and the filled states above the As-atoms.⁴⁹

In order to obtain a complete picture of the electronic structure including the region around the Fermi level, we performed spectroscopic point measurements on the surface, and in Figure 3i we plot differential conductivity that is proportional to LDOS.³³ We extract the band edges by applying linear extrapolations at the onset of conductivity as was proposed by Feenstra.³³ To analyze the spectrum we first notice that the band gap region that stretches from -0.55 to $+2.30$ eV is without states but is at the same time much larger than the reported Wz GaAs band gap of 1.44 – 1.54 .^{13,14,16,50} For unpinned surfaces, it is common to observe an enlarged band gap due to TIBB. TIBB is a phenomenon where some of the applied bias drops in the sample itself acting to bend the bands in the near surface region.^{51,52} TIBB is to a large degree determined by the tip geometry and the charge carrier concentration in the sample. It is important to mention that for a surface experiencing a Fermi level pinning, the charges associated with the pinning would most often be effective in screening the TIBB and therefore reduce its influence, which indicates that the $\{10\bar{1}0\}$ surface studied here is unpinned. We notice that the Fermi level (placed at 0 V sample bias) is shifted toward the valence band edge as it would be for p-type material. From the large TIBB and the nonpolar nature of the surface, we believe that the surface is most probably unpinned and the location of the Fermi level is then an indicator of the “bulk” charge carrier concentration of our NW. Indeed, previous investigations of MOVPE grown undoped GaAs NWs have

shown a tendency for low p-type conductivity,⁵³ as observed in the present investigation.

We then performed atomic scale imaging of the other Wz facet, $\{11\bar{2}0\}$, clearly observing the top layer As lattice. The $\{11\bar{2}0\}$ facet, Figure 4a,b, shows atoms in a zigzag configuration

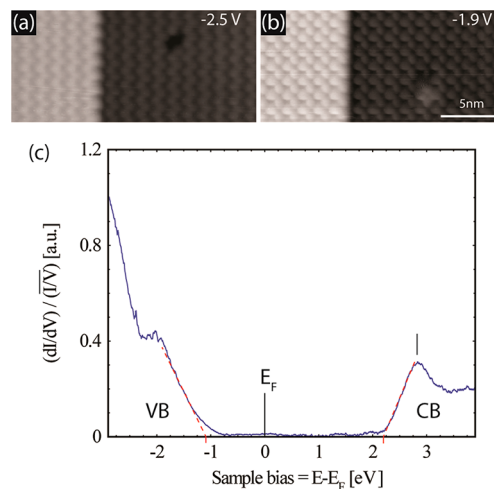


Figure 4. (a,b) STM images of a $\{11\bar{2}0\}$ -type facet using different sample biases as shown in the figure. $I_t = 100$ pA. (c) STS spectrum obtained from a $\{11\bar{2}0\}$ -type facet. The linear onsets marked by the dotted red lines show the valence and conduction band edges. States associated with tunneling out of filled valence band states, VB, and tunneling into empty conduction band states, CB, are marked as well as the Fermi level, E_F . The black line marks a surface state related feature.

indicative of an unreconstructed surface.²³ However, at negative bias imaging we found that when the bias was decreased, that is, using a smaller tip–sample separation, we could see a clear asymmetry in the surface atoms. Every second atom in the zigzag chain appeared larger which is unexpected since the surface atoms should be symmetric. This can be understood as being due to an asymmetry of the STM tip. However, it is worth mentioning that this sensitivity to the shape of the STM tip is again different to the Zb $\{110\}$ facet indicating that the detailed tip–sample interaction is different for the Wz surface as compared to the Zb. From the images, showing the filled states of the sample and thus being sensitive to the As atoms, we can observe the excellent overall homogeneity of the surface with fewer As defects compared to the $\{110\}$ -surface prepared at similar temperatures. Importantly, this indicates a lower energy barrier for As desorption on Zb compared to Wz which is in not unreasonable with a predicted lower surface energies of the Wz facet²⁹ in mind.

We also investigated the electronic structure of the $\{11\bar{2}0\}$ facet using STS. In Figure 4c, we present normalized differential conductance as a function of sample bias. We first notice that the band gap region, which is found between -1.10 and $+2.20$ eV, is also here without states in the band gap but still heavily influenced by TIBB as it stretches over a large voltage range. The overall features in the STS data from the different Wz facets resemble each other to a large degree, but the $\{11\bar{2}0\}$ -type facet showed a larger band gap region, which however might be due to an increased TIBB arising from a blunter tip being used in this case. In addition, the observed valence band position (for p-type material) is well-known to be very sensitive

to the local tip–sample properties⁵⁴ and will shift when using different tips.

For both Wz facets, we found a distinct feature in the spectra at 0.8–0.9 eV above the conduction band edge. This is in good agreement with previous findings on GaAs(110) where this was attributed to be a “surface-state related feature”.³³ The appearance of this feature on three structurally different GaAs surfaces would indicate that it is a very robust state related to the GaAs local chemistry and not the long-range structural order. At roughly 1 eV below the valence band edge, we find a small plateau in the normalized differential conductivity for both Wz facets. For Zb, this plateau has been found to extend over a large energy range,³³ but for our Wz facets we find another increase in LDOS at slightly lower energies which matches well to the predicted occurrence of Wz related bands.²¹ The only clear difference we found between the two Wz facets was the increase in LDOS at roughly 1.2 eV above the conduction band edge for the {1010} facet. This increase was absent for both the {1120}-type as well as for the {110}-type facet⁵⁵ and we can therefore attribute it to be a surface state feature unique to {1010}-type facets.

We continued our STS investigations on neighboring {110} and {1120}-type facets, that is, moving from red to blue in Figure 1b. We made use of the fact that these two facets have a sharp, flat, and well-defined interface and can be accessed without moving across any surface steps, as in the case of Figure 5a. Therefore, we could easily follow the tip movement from one facet to the other and know that the tip geometry was unchanged, a factor that greatly influences the TIBB. Further, we assumed that the charge carrier concentration was similar in both parts since they were grown at the same temperature. We extract the band edges in the same manner as before using linear extrapolations. Once again we found that the TIBB gives rise to an enlarged observed band gap but still with no/few states in the band gap region. For the {1120} facet, we did observe some nonzero conductivity close to the conduction band edge that was attributed to electrons tunneling into unoccupied acceptor states inherent to unintentional carbon doping. Already with the TIBB affecting the measurements we noticed that the band edges for the {110}-type facet were shifted toward more negative values compared to the {1120} facet. We modeled the TIBB using a 3D Poisson solver designed to model the effect of a hyperbolically shaped probe tip in the proximity of a semiconductor.^{56–58} Using reasonable assumptions, a tip with 10 nm curvature, a contact potential difference (work function difference) between tip and sample of 0.6 V, charge carrier concentration of 10^{16} cm^{-3} , and tip–sample distance of 10 Å, we could fit the {110} data to the well-known Zb band gap of 1.42 eV. We then used the same parameters to deduce the band edges for the {1120}-type facet. We assumed nominal Zb values for the conduction band effective mass ($0.0635m_0$), heavy and light hole effective masses ($0.643m_0$ and $0.081m_0$), split-off hole effective mass ($0.172m_0$), dielectric constant (12.9), and spin–orbit splitting (0.348 eV). For the present case with a low NW charge carrier concentration, we note that varying these values significantly did not change the calculated TIBB. Another parameter that is included in the modeling is the band gap, and we modeled the TIBB at the Wz part using band gap values of 1.35–1.55 eV but found that within this range it did not influence the TIBB significantly. To ensure that our determination of the band edges is robust, we also used a slightly different approach where we fitted the band edges according to ref 57 and only found 20

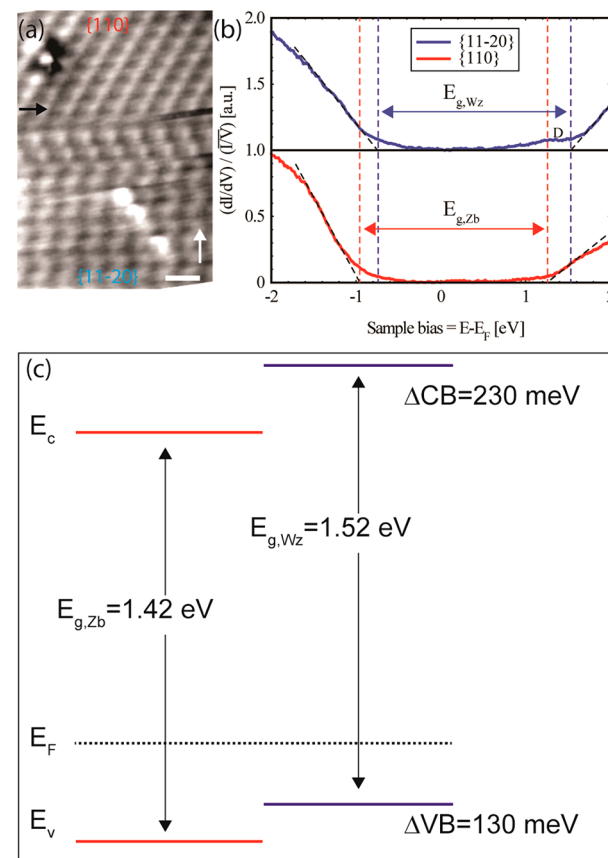


Figure 5. (a) Atomic scale image at the {11-20}-{110} interface region. The bottom part of the image depicts the {11-20}-type Wz facet with its characteristic zigzag appearance. The top part is {110}-type with chains of atoms extending at 35° to [111]. The black arrow marks a twin defect, whereas the white arrow marks the NW growth direction. The scalebar denotes 10 Å. $V_t = -2.7$ V, $I_t = 140$ pA. (b) STS spectra obtained on neighboring {11-20} and {110}-type facets. Each spectrum has been averaged over 10–15 individual spectra. The {11-20} spectrum has been shifted vertically for clarity. The dotted lines mark the measured valence and conduction band edges. D marks dopant induced states. (c) TIBB-corrected band offsets and band gaps for the Zb and Wz, respectively.

meV difference in the VB onset for the Wz facet (before TIBB correction) but no difference at the Wz CB edge nor at the Zb edges. We therefore believe that the band ordering measured here is comparably robust since we also find that the TIBB influences the Wz and Zb in similar manners. Finally, we then reach the important conclusion of a TIBB-corrected band gap of 1.52 eV for the {11-20}-type facet and we found valence and conduction band offsets of $\Delta V_b = 130$ meV and $\Delta C_b = 230$ meV with Zb at more negative energies, Figure 5c. The observed larger valence band offset with Zb shifted by 130 meV toward more negative values matches well with previous findings stating shifts in the same direction of 122,¹³ 84,¹⁸ and 117 meV.²¹ The observed conduction band edge shifted by 230 meV is larger than what has been reported previously, 101,¹³ 117,¹⁸ and 149 meV,²¹ but we do note that the position of the lowest conduction band in Wz GaAs is under debate as it has been reported to experience both Γ_7 ^{15,21} and Γ_8 ²⁰ symmetry. In STM, we integrate the tunneling signal over all k -vectors and can therefore not definitely determine the conduction band ordering. It is, however, apparent that we measure a band gap

of Wz GaAs that is larger than the corresponding Zb band gap that would support the previous reports of a Γ_{7c} symmetry.^{15,21}

In conclusion, we have performed scanning tunneling microscopy and spectroscopy measurements on GaAs NWs with axial stacking of Wz and Zb segments. Atomic scale images were obtained from {110}, {1010}, and {1120}-type facets showing unreconstructed surfaces. Scanning tunneling spectroscopy revealed surfaces free from states in the band gap region but also significant tip induced band bending. The Fermi level placement indicated that the NWs had low p-type conductivity as has previously been seen for other MOVPE grown GaAs NWs. By modeling the TIBB, we could extract a type-II staggered band alignment with Zb at more negative energies and a 100 meV larger band gap for Wz GaAs supporting recent electronic structure simulations. This is the first successful STM/S-based study of band offsets in III–V NWs, and we note that previous attempts in other III–V systems encountered challenges not observed here: (i) For InAs Wz surfaces we have previously observed a band gap region with step-induced states²³ making band extractions impossible. (ii) For the InP NW system we found surfaces that were Fermi level pinned masking the bulk band offsets.²⁴ The lack of states in the band gap and the unpinned nature of the Wz GaAs surfaces, however, make it an ideal candidate for band offset determination by STS, proving the strength of the method as a novel tool for electronic structure determination in NWs beyond the surface region. The experiments prove the versatility of the STM as a direct probe for atomic as well as electronic structure of III–V nanostructures reaching beyond the surface region. The findings allow for new NW based research and technology, for example, studies of crystal phase quantum dots, surface modifications, and investigations of adsorbed species on NW surfaces.

■ ASSOCIATED CONTENT

Supporting Information

Sample preparation, Figures S1–S2. This material is available free of charge via the Internet at <http://pubs.acs.org>.

■ AUTHOR INFORMATION

Corresponding Author

*E-mail: anders.mikkelsen@sljus.lu.se.

Notes

The authors declare no competing financial interest.

■ ACKNOWLEDGMENTS

This work was performed within the Nanometer Structure Consortium at Lund University (nmC@LU), and was supported by the Swedish Research Council (VR), the Swedish Foundation for Strategic Research (SSF), the Swedish energy agency, the Crafoord Foundation, the Knut and Alice Wallenberg Foundation, and the European Research Council under the European Union's Seventh Framework Programme Grant Agreement 259141. One of the authors (R.T.) acknowledges support from the European Commission under a Marie Curie Intra-European Fellowship. S.L. gratefully acknowledges the support by a fellowship within the Postdoc-Programme of the German Academic Exchange Service (DAAD). This report is based on a project that was funded by E.ON AG as part of the E.ON International Research Initiative.

■ REFERENCES

- (1) Heiss, M.; Fontana, Y.; Gustafsson, A.; Wüst, G.; Magen, C.; O'Regan, D. D.; Luo, J. W.; Ketterer, B.; Conesa-Boj, S.; Kuhlmann, A. V.; Houel, J.; Russo-Averchi, E.; Morante, J. R.; Cantoni, M.; Marzari, N.; Arbiol, J.; Zunger, A.; Warburton, R. J.; Fontcuberta i Morral, A. *Nat. Mater.* **2013**, *12*, 439–444.
- (2) Heurlin, M.; Magnusson, M. H.; Lindgren, D.; Ek, M.; Wallenberg, L. R.; Deppert, K.; Samuelson, L. *Nature* **2012**, *492* (7427), 90–94.
- (3) Mariani, G.; Scofield, A. C.; Hung, C.-H.; Huffaker, D. L. *Nat. Commun.* **2013**, *4*, 1497.
- (4) Joyce, H. J.; Wong-Leung, J.; Gao, Q.; Tan, H. H.; Jagadish, C. *Nano Lett.* **2010**, *10* (3), 908–915.
- (5) Lehmann, S.; Jacobsson, D.; Deppert, K.; Dick, K. *Nano Res.* **2012**, *5*, 470–476.
- (6) Algra, R. E.; Verheijen, M. A.; Borgström, M. T.; Feiner, L. F.; Immink, G.; van Enckevort, W. J. P.; Vlieg, E.; Bakkers, E. P. A. M. *Nature* **2008**, *456* (7220), 369–372.
- (7) Caroff, P.; Dick, K. A.; Johansson, J.; Messing, M. E.; Deppert, K.; Samuelson, L. *Nat. Nanotechnol.* **2009**, *4* (1), 50–55.
- (8) Dick, K. A.; Thelander, C.; Samuelson, L.; Caroff, P. *Nano Lett.* **2010**, *10* (9), 3494–3499.
- (9) Akopian, N.; Patriarche, G.; Liu, L.; Harmand, J. C.; Zwiller, V. *Nano Lett.* **2010**, *10* (4), 1198–1201.
- (10) Caroff, P.; Bolinsson, J.; Johansson, J. *IEEE J. Sel. Top. Quantum Electron.* **2011**, *17* (4), 829–846.
- (11) Spirkoska, D.; Arbiol, J.; Gustafsson, A.; Conesa-Boj, S.; Glas, F.; Zardo, I.; Heigoldt, M.; Gass, M. H.; Bleloch, A. L.; Estrade, S.; Kaniber, M.; Rossler, J.; Peiro, F.; Morante, J. R.; Abstreiter, G.; Samuelson, L.; Fontcuberta i Morral, A. *Phys. Rev. B* **2009**, *80* (24), 245325.
- (12) Kim, D. C.; Dheeraj, D. L.; Fimland, B. O.; Weman, H. *Appl. Phys. Lett.* **2013**, *102* (14), 142107–5.
- (13) Heiss, M.; Conesa-Boj, S.; Ren, J.; Tseng, H.-H.; Gali, A.; Rudolph, A.; Uccelli, E.; Peiró, F.; Morante, J. R.; Schuh, D.; Reiger, E.; Kaxiras, E.; Arbiol, J.; Fontcuberta i Morral, A. *Phys. Rev. B* **2011**, *83* (4), 045303.
- (14) Hoang, T. B.; Moses, A. F.; Zhou, H. L.; Dheeraj, D. L.; Fimland, B. O.; Weman, H. *Appl. Phys. Lett.* **2009**, *94* (13), 133105–3.
- (15) Ketterer, B.; Heiss, M.; Uccelli, E.; Arbiol, J.; Fontcuberta i Morral, A. *ACS Nano* **2011**, *5* (9), 7585–7592.
- (16) Ahtapodov, L.; Todorovic, J.; Olk, P.; Mjåland, T.; Slåttnes, P.; Dheeraj, D. L.; van Helvoort, A. T. J.; Fimland, B.-O.; Weman, H. *Nano Lett.* **2012**, *12* (12), 6090–6095.
- (17) Zanolli, Z.; Fuchs, F.; Furthmüller, J.; von Barth, U.; Bechstedt, F. *Phys. Rev. B* **2007**, *75* (24), 245121.
- (18) Murayama, M.; Nakayama, T. *Phys. Rev. B* **1994**, *49* (7), 4710–4724.
- (19) Yeh, C.-Y.; Wei, S.-H.; Zunger, A. *Phys. Rev. B* **1994**, *50* (4), 2715–2718.
- (20) De, A.; Pryor, C. E. *Phys. Rev. B* **2010**, *81* (15), 155210.
- (21) Belabbes, A.; Panse, C.; Furthmüller, J.; Bechstedt, F. *Phys. Rev. B* **2012**, *86* (7), 075208.
- (22) Xu, T.; Dick, K. A.; Plissard, S.; Nguyen, T. H.; Makoudi, Y.; Berthe, M.; Nys, J. P.; Wallart, X.; Grandidier, B.; Caroff, P. *Nanotechnology* **2012**, *23*, 095702.
- (23) Hilner, E.; Håkanson, U.; Fröberg, L. E.; Karlsson, M.; Kratzer, P.; Lundgren, E.; Samuelson, L.; Mikkelsen, A. *Nano Lett.* **2008**, *8* (11), 3978–3982.
- (24) Hjort, M.; Wallentin, J.; Timm, R.; Zakharov, A. A.; Håkanson, U.; Andersen, J. N.; Lundgren, E.; Samuelson, L.; Borgström, M. T.; Mikkelsen, A. *AcS Nano* **2012**, *6*, 9679.
- (25) Yu, E. T. *Chem. Rev.* **1997**, *97* (4), 1017–1044.
- (26) Mikkelsen, A.; Lundgren, E. *Prog. Surf. Sci.* **2005**, *80* (1–2), 1–25.
- (27) Feenstra, R. M. *Semicond. Sci. Technol.* **1994**, *9* (12), 2157.
- (28) Timm, R.; Eisele, H.; Lenz, A.; Ivanova, L.; Vosseburger, V.; Warming, T.; Bimberg, D.; Farrer, I.; Ritchie, D. A.; Dähne, M. *Nano Lett.* **2010**, *10* (10), 3972–3977.

- (29) Pankoke, V.; Kratzer, P.; Sakong, S. *Phys. Rev. B* **2011**, *84* (7), 075455.
- (30) Ghalamestani, S. G.; Heurlin, M.; Wernersson, L.-E.; Lehmann, S.; Dick, K. A. *Nanotechnology* **2012**, *23* (28), 285601.
- (31) Lehmann, S. *Nano Lett.* **2013**, DOI: 10.1021/nl401554w.
- (32) Magnusson, M. H.; Deppert, K.; Malm, J.-O.; Bovin, J.-O.; Samuelson, L. *Nanostruct. Mater.* **1999**, *12* (1–4), 45–48.
- (33) Feenstra, R. M. *Phys. Rev. B* **1994**, *50* (7), 4561–4570.
- (34) Martensson, P.; Feenstra, R. M. *Phys. Rev. B* **1989**, *39* (11), 7744–7753.
- (35) Lang, N. D. *Phys. Rev. B* **1986**, *34* (8), 5947–5950.
- (36) Feenstra, R. M.; Stroscio, J. A.; Fein, A. P. *Surf. Sci.* **1987**, *181* (1–2), 295–306.
- (37) Thornton, J. M. C.; Woolf, D. A.; Weightman, P. *Appl. Surf. Sci.* **1998**, *123–124* (0), 115–119.
- (38) Knutsson, J.; Lehmann, S.; Hjort, M.; Timm, R.; Dick, K. A.; Mikkelsen, A. Lund University, Lund, Sweden. Unpublished work, 2013.
- (39) Jenichen, A.; Engler, C.; Rauschenbach, B. *Surf. Sci.* **2013**, *613*, 74–79.
- (40) Ugeda, M. M.; Brihuega, I.; Guinea, F.; Gómez-Rodríguez, J. M. *Phys. Rev. Lett.* **2010**, *104* (9), 096804.
- (41) Heinrich, M.; Domke, C.; Ebert, P.; Urban, K. *Phys. Rev. B* **1996**, *53* (16), 10894–10897.
- (42) Gaan, S.; Feenstra, R. M.; Ebert, P.; Dunin-Borkowski, R. E.; Walker, J.; Towe, E. *Surf. Sci.* **2012**, *606* (1–2), 28–33.
- (43) Siemens, B.; Domke, C.; Ebert, P.; Urban, K. *Phys. Rev. B* **1999**, *59* (4), 3000–3007.
- (44) Ebert, P.; Engels, B.; Richard, P.; Schroeder, K.; Blügel, S.; Domke, C.; Heinrich, M.; Urban, K. *Phys. Rev. Lett.* **1996**, *77* (14), 2997–3000.
- (45) de Raad, G. J.; Bruls, D. M.; Koenraad, P. M.; Wolter, J. H. *Phys Rev B* **2002**, *66* (19), 195306.
- (46) Jäger, N. D.; Ebert, P.; Urban, K.; Krause-Rehberg, R.; Weber, E. R. *Phys Rev B* **2002**, *65* (19), 195318.
- (47) Heinrich, A. J.; Wenderoth, M.; Rosentreter, M. A.; Schneider, M. A.; Ulbrich, R. G. *Appl. Phys. Lett.* **1997**, *70* (4), 449–451.
- (48) de Raad, G. J.; Bruls, D. M.; Koenraad, P. M.; Wolter, J. H. *Phys. Rev. B* **2001**, *64* (7), 075314.
- (49) Feenstra, R. M.; Stroscio, J. A.; Tersoff, J.; Fein, A. P. *Phys. Rev. Lett.* **1987**, *58* (12), 1192–1195.
- (50) Martelli, F.; Piccin, M.; Bais, G.; Jabeen, F.; Ambrosini, S.; Rubini, S.; Franciosi, A. *Nanotechnology* **2007**, *18* (12), 125603.
- (51) Timm, R.; Feenstra, R. M.; Eisele, H.; Lenz, A.; Ivanova, L.; Lenz, E.; Dähne, M. *J. Appl. Phys.* **2009**, *105*, 093718.
- (52) Feenstra, R. M.; Dong, Y.; Semtsiv, M. P.; Masselink, W. T. *Nanotechnology* **2007**, *18* (4), 044015.
- (53) Regolin, I.; Gutsche, C.; Lysov, A.; Blekker, K.; Li, Z.-A.; Spasova, M.; Prost, W.; Tegude, F. J. *J. Cryst. Growth* **2011**, *315* (1), 143–147.
- (54) Jäger, N. D.; Urban, K.; Weber, E. R.; Ebert, P. *Appl. Phys. Lett.* **2003**, *82* (16), 2700–2702.
- (55) Feenstra, R. M.; Meyer, G.; Moresco, F.; Rieder, K. H. *Phys Rev B* **2002**, *66*, 165204.
- (56) SEMITIP software. http://www.andrew.cmu.edu/user/feenstra/semitip_v6/ (accessed April 1, 2013).
- (57) Feenstra, R. M.; Lee, J. Y.; Kang, M. H.; Meyer, G.; Rieder, K. H. *Phys. Rev. B* **2006**, *73*, 035310.
- (58) Feenstra, R. M.; Stroscio, J. A. *J. Vac. Sci. Technol., B* **1987**, *5* (4), 923–929.